Single axis FOG aided attitude estimation algorithm for mobile robots

B. Allotta*°, R. Costanzi*°, F. Fanelli*°, N. Monni*°, A. Ridolfi*°

University of Florence
Department of Industrial Engineering (DIEF)
Via di Santa Marta 3, 50139, Florence, Italy
Tel.: +39-055-2758764
Fax: +39-055-2758755
emails: a.ridolfi@unifi.it, riccardo.costanzi@unifi.it

° ISME Interuniversity Center of Integrated Systems for the Marine Environment
www.isme.unige.it

Abstract

This paper is focused on an attitude estimation method for Autonomous Underwater Vehicles (AUVs). Data acquired by a commercial Micro-Electro-Mechanical Systems (MEMS) Inertial Measurement Unit (IMU), equipped with magnetometers, and a Fibre Optic Gyroscope (FOG) are fused to estimate the attitude of the vehicle. One of the most used attitude estimation filter, a Nonlinear Complementary Filter (NCF), is proposed as the basis of this work; then, some adaptations to the original formulation of the filter are illustrated to better suit it to the field of underwater robotics. The proposed improvements include the online tuning of the gains of the filter to cope with sensor disturbances and the employment of the data acquired by a FOG. In addition, a fast procedure for the calibration of a magnetometer is introduced to increase the reliability of its readings. The resulting filter is used to estimate the attitude of an AUV; the performances of the proposed solution are tested and evaluated, in particular when unpredictable magnetic disturbances are present, highlighting the improvements that the applied changes allow to achieve in the specific field of application.

Keywords: Attitude estimation, complementary filter, underwater robotics, AUV.

1. Introduction

Nowadays, Inertial Navigation Systems (INS) are widely used in many fields of application. The diffusion of Micro-Electro-Mechanical Systems (MEMS) caused the spread of low cost and lightweight Inertial Measurement Units (IMUs), which are employed in a wide range of industrial sectors.
A typical application is navigation aid of terrestrial, maritime and aerial vehicles, where IMUs play an important role in achieving accurate pose and velocity estimates.
This paper focuses on IMU use for attitude estimation **of mobile robots, with particular regards to the field of underwater robotics.** The underwater environment poses an additional challenge due to the nature of the surrounding fluid, reducing the number of sensors available for a correct estimation.
In the selected case study, sensor readings are exploited to compute an accurate estimate of the orientation of an Autonomous Underwater Vehicle (AUV) equipped with an IMU comprised of a 3-axis gyroscope, a 3-axis accelerometer and a 3-axis magnetometer. A suitable estimation filter has been employed to correctly fuse data coming from different sensors and to give a precise estimate of the current attitude of the vehicle. **Special attention has been dedicated to the estimation of the yaw angle (which measures the orientation of the vehicle with respect to the North, and which is particularly susceptible to external magnetic disturbances), whose correct estimate is indeed of fundamental importance to an AUV, to achieve limited errors during navigation.**
Several filtering techniques have been studied during the years and many sources can be found in literature (e.g. [1], [2], [3], [4], [5], [6], [7], [8]). The classic approach consists in the use of a Kalman filter [9] and their nonlinear counterparts, such as the Extended Kalman Filter (EKF) or the Unscented Kalman Filter (UKF) [10], [11]. A valid alternative is the use of linear complementary filters: such filters can be used to fuse measurements of different signals that possess complementary spectral characteristics [12]. One of the most important contributes on the subject has been given in 2008 by Mahony et al. [13]. Mahony's Nonlinear Explicit Complementary Filter (NECF in the following), whose name is due to the architectural

similarity with the aforementioned linear complementary filters, has become a standard reference in the field.

This paper uses the NECF as a basis, and proposes a set of design modifications with the purpose to better adapt it to estimate the attitude of an underwater robot. **These changes, justified by the characteristics of the underwater environment and by the limitations imposed by the adopted sensors, are aimed at adapting the existing NECF to concrete application (in particular in the underwater field); hence, the proposed modifications are more related to practical experimentation than to theoretical aspects.**

A magnetometer calibration algorithm, applicable when the rotation of the vehicle is limited, is proposed in the paper: calibration must be performed to increase the reliability of the readings of the sensor prior to the estimation process. Furthermore, to better cope with magnetic disturbances caused by metal objects (**whose presence is not uncommon in the underwater environment: for example, industrial platforms can induce severe magnetic field disturbances; in addition, if AUVs are used for seabed inspection tasks, metal debris due to modern wrecks may strongly affect the compass readings**) one of the proposed design changes include the integration of a single-axis Fibre Optic Gyroscope (FOG), that can greatly improve the accuracy of the computed estimate in the presence of external magnetic sources. **Experimental sea trials have been executed to test the proposed strategy and to validate the applied design changes to the original formulation of the NECF;** the achieved results are promising, especially in the presence of magnetic disturbances.

The paper is organized as follows: Section 2 introduces the considered IMU sensor configuration, illustrating the equations used to model the sensors behavior; Section 3 presents the algorithm used to calibrate the magnetometer. Then, Section 4 is dedicated to the NECF: at first the classic structure of the filter is introduced; subsequently, the applied design changes are explained. The performances of the resulting filter have been evaluated during suitable tests where it is employed to estimate the attitude of an AUV, comparing the output of the filter with the estimate given by a commercial IMU internal algorithm; the results obtained are presented in Section 5.

2. IMU description

The IMU considered in this paper is composed of a 3-axis gyroscope, a 3-axis magnetometer and a 3-axis accelerometer. Let $\{B\}$ denote the body frame (attached to the sensor), and let $R = R_B^I$ denote the rotation matrix that describes the attitude of the body frame with respect to the inertial frame $\{I\}$ (from which a suitable triplet of Euler angles, such as *roll*, *pitch* and *yaw* angles, can be extracted). The following error models are used for the sensors:

- *Gyroscope*:

$$\boldsymbol{\omega}_m^B = \boldsymbol{\omega}^B + \mathbf{b}_g + \boldsymbol{\mu}_g \ , \tag{1}$$

where the measured quantity $\boldsymbol{\omega}_m^B$ is the sum of the true angular velocity $\boldsymbol{\omega}^B$ (expressed in the body frame), a time-varying bias $\boldsymbol{b}_g$ and additional measurement noise $\boldsymbol{\mu}_g$.

- *Magnetometer*:

$$\mathbf{m}_m^B = W R^T \mathbf{H}^I + \mathbf{H}_d + \boldsymbol{\mu}_m \ , \tag{2}$$

being $\mathbf{H}^I$ the Earth's magnetic field expressed in the inertial frame, W and $\mathbf{H}_d$ represent the disturbances due to local magnetic interferences (whose effect will be analysed in Section 3) and $\boldsymbol{\mu}_m$ is measurement noise.

- *Accelerometer*:

$$\mathbf{a}_m^B = R^T \mathbf{a}^I + \mathbf{b}_a + \boldsymbol{\mu}_a \ , \tag{3}$$

where $\boldsymbol{\mu}_a$ represents measurement noise and $\mathbf{b}_a$ is the accelerometer bias, responsible for a shift of the acceleration vector from its true direction; **in this context, the bias term is assumed to be zero**. Vector $\mathbf{a}^I$, expressed in the inertial frame, is the sum of $\dot{\mathbf{v}}^I$, which is the time derivative of the linear velocity of the device $\mathbf{v}^I$, and of the gravitational acceleration $\mathbf{g}$. However, for the considered field of application, the accelerations are usually very small; hence, vector $\mathbf{a}_m^B$ constitutes a good approximation of the inertial vertical axis expressed in the body frame.

In the considered case study, the IMU is mounted with its x-axis aligned with the direction of forward motion of the vehicle and the z-axis pointing down, and the attitude estimate is computed with respect to a *North East Down* (NED) inertial frame.

3. Magnetometer calibration

A 3-axis magnetometer measures the direction and the intensity of the total magnetic field around the device. It cannot, however, distinguish between the Earth's magnetic field and additive magnetic disturbances.

The Earth's magnetic field vector direction depends on the geographical location; however, over the operating area of an underwater vehicle, it can be considered constant and known with respect to the inertial frame. In the absence of disturbances, the measurements obtained by arbitrarily rotating the sensor in 3D space would lie on the surface of a sphere centered at the origin of the body frame and whose radius is the magnitude of the field at the geographic location where such operation is performed. However, in the presence of magnets or ferromagnetic objects, the measurements are distorted. Note that only disturbances which rotate together with the sensors are taken into account, as

these disturbances are the only ones that can be compensated during the calibration phase.

In this paper, the considered error model is expressed in Eq. (2): magnetic disturbances add bias and scaling of the output. Separating the two effects, we can distinguish between:

- *Hard Iron disturbances*:
  Permanent magnets and magnetized objects, such as electronic subsystems in the proximity of the sensor, cause the so-called "Hard Iron effect": these objects are the source of a permanent magnetic field, constant in all directions. They have the effect of adding a bias $\mathbf{H}_d$ on the magnetometer output. While permanent magnets generate a constant magnetic field, the field generated by electronic subsystems close to the sensor varies with the DC current flowing in the wires; however, since the magnetometer calibration procedure is executed at the beginning of a navigation mission, a constant value for the bias $\mathbf{H}_d$ has been considered, assuming that the generated magnetic field will not undergo relevant variations.

- *Soft Iron disturbances*:
  Matrix W in Eq. (2) represents the "Soft Iron effect": ferromagnetic materials close to the sensor (such as iron and nickel) produce a local magnetic field, whose magnitude is related to the angle of incidence of Earth's magnetic field on the material itself. Hence, this effect changes when the sensor rotates, and it has the consequence of deforming the sphere of measurements into an ellipsoid tilted in 3D space along an arbitrary axis.

If both kinds of disturbance are present, the measurements taken while rotating the sensor in space would lie on the surface of an ellipsoid (due to W) centered at a certain offset from the origin (due to Hard Iron effect).

For example, Figure 1 shows the magnetometer readings taken while rotating the device in 3D space in a disturbance-free environment; it is easy to note that the measurements lie with good approximation on the surface of a sphere (actually, the radius of the sphere does not reflect the true magnitude of the magnetic field, since the sensor readings are given in **arbitrary units**). On the contrary, Figure 2 reports the measurements of the magnetometer taken in the same geographical locality as in the previous test, but after attaching metal objects to the sensor case: in this case, the previously obtained sphere is deformed, and its centre is shifted away from the origin of the sensor frame.

Complete three-dimensional magnetometer calibration procedures consist of estimating the matrix W and the offset $\mathbf{H}_d$, in order to correctly map every subsequent measurement on the surface of the theoretical sphere, even in the presence of external magnetic fields.

The most common calibration techniques are based on ellipsoid fitting [26] after collecting measurements while ro-
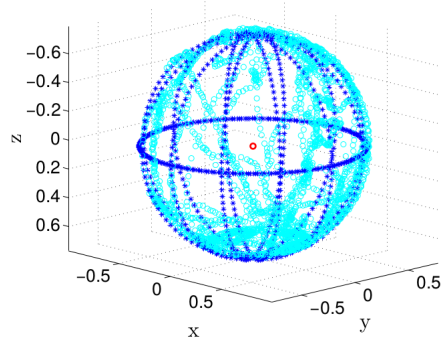

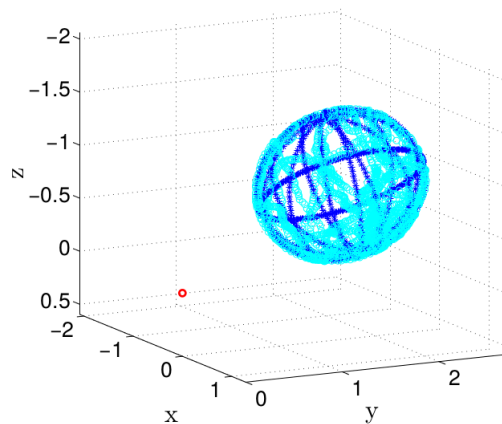Figure 1: Magnetometer readings with no magnetic disturbances.

Figure 2: Magnetometer readings with magnetic disturbances.

tating the sensor in a sufficient number of different orientations in 3D space, the best fitting ellipsoid (in a least square sense) can be found; once its center, radii and axes are known, the offset $\mathbf{H}_d$ and the scaling W can be corrected.

While these techniques are fairly simple, computationally efficient, and prove to be efficient in a large number of situations, they are not applicable when the sensor rotation along one (or more) axis is constrained. This is the case of the considered field of application: the roll and pitch angles (rotation along x-axis and y-axis, respectively) of an autonomous underwater vehicle are typically limited to a strict range (because of the hydrostatic stability of the vehicle). This restriction implies that the set of measurements to be used for the calibration procedure does not usually include enough information content along one space dimension (the vertical direction) to completely identify the shape of the ellipsoid.

Tests in a controlled environment have been conducted to verify if, by executing a complete yaw turn of the vehicle, measurements would be sufficient to correctly fit the data to an ellipsoid. However, even in the presence of currents, which cause the rotation of the vehicle with respect to the horizontal plane, ellipsoid fitting has not been proven to be a reliable technique to estimate the locus of the magnetometer measurements. This reflects the impossibility of determining an ellipsoid from an (almost) elliptical data

set.

Hence, the goal is to find a simple and fast calibration technique which can approximate at best the theoretical locus on which the uncorrupted measurements lie, using only data, which roughly lie on a plane, acquired during a complete turn of the vehicle along its z-axis.

During the calibration turn, it is especially important that the roll and the pitch angles of the vehicle remain close to zero; the following characteristics are exploited to ensure the horizontality of the AUV in all scenarios (e.g. even in case of bad weather and sea conditions):

- geometrical shape: the long and slender shape of the AUV ("torpedo-shape"), which dampens the pitch rotations;

- pitch control: the pitch degree of freedom is actively controlled, thus guaranteeing limited values for such angle if proper reference signals are applied. The Typhoon AUV is indeed controlled to navigate basically on a horizontal plane (e.g. when diving, this AUV exploits its vertical thrusters and thus vertically translates);

- hydrostatic stability: the correct positioning and alignment of the centers of buoyancy and gravity ensures limited roll and pitch motions and increases the overall stability of the vehicle.

The idea behind the calibration algorithm proposed in this paper is to perform a planar ellipse fit (the only one available when roll and pitch angles are constrained) on the data set constituted of the complete magnetometer readings.

The illustrated technique is exact if the measurements are taken while the vehicle is horizontal, and remains sufficiently reliable for small roll and pitch angles values (within the usual ranges for an AUV). If used in conjunction with the magnetometer's gain choice strategy presented in Section 4.2.3 and an accurate gyroscope (e.g. a FOG), it is good enough to obtain a reliable attitude estimate.

Let us assume that the x-axis of the NED reference frame is pointing towards magnetic north; then, on every point of the Earth's surface (exception made for the magnetic poles) the Earth's magnetic field has two nonzero components: one in the North-South direction (H_x^I) and a component directed towards the Earth's center (vertical component H_z^I). Since these components are known at each location, and can be easily computed using online calculators (e.g. [29]), the locus given by measurements taken on the horizontal plane is a well identifiable circle on the theoretical magnetic field sphere: it is indeed a circle whose axis is parallel with the z-axis of the sensor, whose center is on such axis at the height of H_z^I and whose radius is given by $r = H_x^I$. Figure 3 is given for a better understanding.

Note that, if the x-axis of the considered NED frame is directed towards geographic North instead (also known as "true North") a third East-West nonzero component of the Earth's magnetic field is present (H_y^I), while the intensity of H_x^I is reduced and r must be computed as $r = \sqrt{(H_x^I)^2 + (H_y^I)^2}$; this is because magnetic and geographic North do not coincide (the angular difference between the two points is known as "magnetic declination"). If
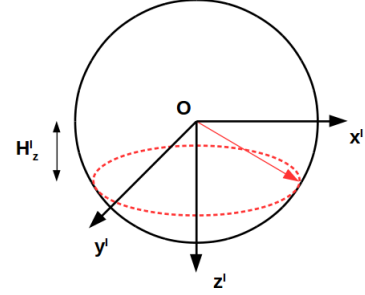

Figure 3: Magnetic field measurements on the horizontal plane.

both hard and soft iron disturbances are present, the circle in Fig. 3 is mapped onto an ellipse which is arbitrarily rotated in the space (see Fig. 4). The idea behind the proposed calibration procedure is to compare the circular locus of measurements on the horizontal plane with the ellipse it is deformed into by magnetic disturbances, in order to determine the transformation that maps the former onto the latter and to compensate the disturbances by applying the inverse transformation to the magnetometer readings.
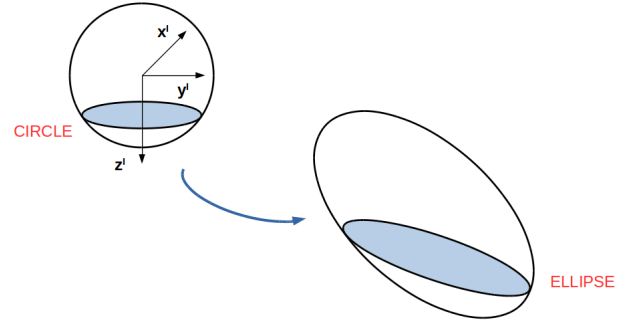

Figure 4: Magnetic field measurements locus deformation in the presence of both hard and soft iron magnetic disturbances.

The algorithm is composed of the following steps: firstly, the measurement ellipse is rotated so that it lies on a horizontal plane; then, a planar ellipse fitting procedure is applied to determine the center, the radii and the tilt of the ellipse; finally, these quantities are compensated and the measurements are mapped back to the theoretical circle.

Generally, not all the measurements are exactly taken at zero pitch and roll angles; hence, the magnetometer readings do not perfectly lie on a plane. The first step of the calibration algorithm consists in computing the minimal
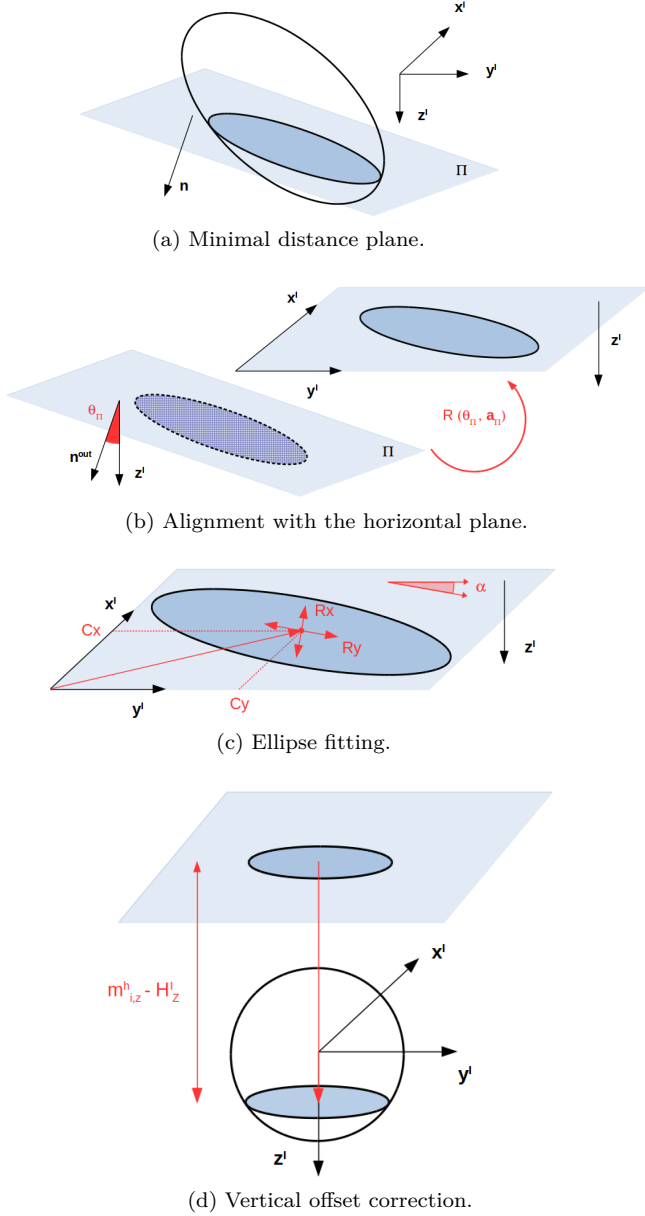
4

(a) Minimal distance plane.

(b) Alignment with the horizontal plane.

(c) Ellipse fitting.

(d) Vertical offset correction.

Figure 5: Magnetometer calibration procedure.

distance plane (in a least square sense) Π that best fits all the points (Fig. 5a). Such calculation can be executed resorting to linear algebra. Consider the standard plane equation

$$ax + by + cz + d = 0 . \tag{4}$$

Let $\mathbf{q} = [x\ y\ z\ 1]^T$ denote a point on the plane, represented as an augmented vector. The vector $\mathbf{A} = [a\ b\ c\ d]^T$ contains the unknowns of the problem. If point $\mathbf{q}$ lies on the plane, it verifies the following equation:

$$\mathbf{q}^T \mathbf{A} = 0 . \tag{5}$$

Given N points (the magnetometer readings), the following linear system can be written:

$$Q\mathbf{A} = \mathbf{e} , \tag{6}$$

where

$$Q = \begin{bmatrix} x_1 & y_1 & z_1 & 1 \\ \vdots & \vdots & \vdots & \vdots \\ x_i & y_i & z_i & 1 \\ \vdots & \vdots & \vdots & \vdots \\ x_N & y_N & z_N & 1 \end{bmatrix} , \tag{7}$$

being each $[x_i\ y_i\ z_i]^T$ a different reading, and $\mathbf{e}$ a $N \times 1$ vector representing the error to be minimized (if all points lie on the plane, then $\mathbf{e} = \mathbf{0} \in \mathbb{R}^{N \times 1}$). The solution of such system is the closest vector to the kernel of Q, which is given by the right-singular vector corresponding to the minimum singular value obtained from the singular value decomposition of Q.

The direction of the normal to the plane is given by $\mathbf{n} = [a\ b\ c]^T$; the position of a point $\mathbf{p}$ on the plane can be found by assigning two coordinates and determining the third one by inverting Eq. (4). The projection of a generic magnetometer reading $\mathbf{m}_i = [x_i\ y_i\ z_i]^T$ on Π is then given by:

$$\mathbf{m}_i^\Pi = [x_i^\Pi\ y_i^\Pi\ z_i^\Pi]^T = \mathbf{m}_i - \left(\mathbf{n}^T (\mathbf{m}_i - \mathbf{p})\right)\ \mathbf{n} . \tag{8}$$

The following step consists in determining the necessary rotation to align Π with the horizontal plane. The "outwards" pointing normal $\mathbf{n}^{out}$ (pointing towards the half-space which does not contain the origin of the axes) is determined: since Eq. (4) is invariant with respect to a constant scale factor, $\mathbf{n}^{out}$ can be either $\mathbf{n}$ or $-\mathbf{n}$; hence, (4) can not be used to determine the correct direction of $\mathbf{n}^{out}$. This indeterminacy can be solved by computing $\mathbf{n}^{out}$ as follows:

$$\mathbf{n}^{out} = \pm \frac{\left((\mathbf{m}_3^\Pi - \mathbf{m}_1^\Pi) \times (\mathbf{m}_2^\Pi - \mathbf{m}_1^\Pi)\right)}{||(\mathbf{m}_3^\Pi - \mathbf{m}_1^\Pi) \times (\mathbf{m}_2^\Pi - \mathbf{m}_1^\Pi)||} , \tag{9}$$

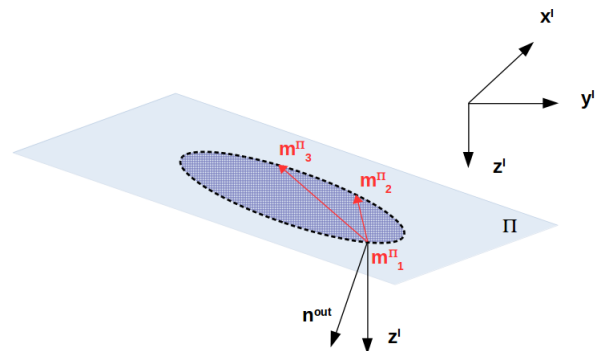where $\times$ indicates the cross-product of vectors. The sign

Figure 6: Computation of $\mathbf{n}^{out}$.

is chosen positive if points $\mathbf{m}_1^\Pi$, $\mathbf{m}_2^\Pi$ and $\mathbf{m}_3^\Pi$ lie counterclockwise on the contour of the ellipse (see Figure 6); this condition can be verified considering the sign of the angle obtained by integrating the gyroscope z-axis reading during the calibration turn.

Let $\mathbf{z}^I = [0\ 0\ 1]^T$ denote the inertial z-axis; in order to

align Π with the horizontal plane, it is necessary to rotate such plane of the angle given by

$$\theta_\Pi = \cos^{-1}\left(\left(\mathbf{z}^I\right)^T \mathbf{n}^{out}\right) \tag{10}$$

about the axis whose direction can be computed with the cross-product:

$$\mathbf{a}_\Pi = \mathbf{n}^{out} \times \mathbf{z}^I . \tag{11}$$

θ_Π and $\mathbf{a}_\Pi$ can be used to compute a suitable rotation matrix $R(\theta_\Pi, \mathbf{a}_\Pi)$ resorting to axis-angle parametrization of rotations [23], which is then applied to the projected points (Fig. 5b):

$$\mathbf{m}_i^h = R(\theta_\Pi, \mathbf{a}_\Pi)\mathbf{m}_i^\Pi . \tag{12}$$

Then, a standard ellipse fitting procedure can be applied to determine the best fitting ellipse (in a least square sense) to the points (Fig. 5c). Without going into details (see [27], [28] for theoretical proof), given the ellipse defined by the implicit equation

$$Ax^2 + Bxy + Cy^2 + Dx + Ey + F = 0 \tag{13}$$

and a set of M different points $m_i^h = [m_{i,x}^h \ m_{i,y}^h \ m_{i,z}^h]^T$, $i = 1, \cdots, M$, the best fitting ellipse is obtained by solving the following generalized eigenvalue problem:

$$S\mathbf{X} = \lambda K\mathbf{X} \tag{14}$$

$$\mathbf{X}^T K \mathbf{X} = 1 , \tag{15}$$

where $\mathbf{X} = [A\ B\ C\ D\ E\ F]^T$ is the vector of unknowns (the coefficients of the ellipse equation), λ is a scalar value, S is the scatter matrix built from measurement:

$$S = Y^T Y \in \mathbb{R}^{M \times 1} \tag{16}$$

$$Y = \begin{bmatrix} (m_{1,x}^h)^2 & m_{1,x}^h m_{1,y}^h & (m_{1,y}^h)^2 & m_{1,x}^h & m_{1,y}^h & 1 \\ \vdots & \vdots & \vdots & \vdots & \vdots & \vdots \\ (m_{i,x}^h)^2 & m_{i,x}^h m_{i,y}^h & (m_{i,y}^h)^2 & m_{i,x}^h & m_{i,y}^h & 1 \\ \vdots & \vdots & \vdots & \vdots & \vdots & \vdots \\ (m_{M,x}^h)^2 & m_{M,x}^h m_{M,y}^h & (m_{M,y}^h)^2 & m_{M,x}^h & m_{M,y}^h & 1 \end{bmatrix} , \tag{17}$$

and K is the constraint matrix defined as follows:

$$K = \begin{bmatrix} 0 & 0 & 2 & 0 & 0 & 0 \\ 0 & -1 & 0 & 0 & 0 & 0 \\ 2 & 0 & 0 & 0 & 0 & 0 \\ 0 & 0 & 0 & 0 & 0 & 0 \\ 0 & 0 & 0 & 0 & 0 & 0 \\ 0 & 0 & 0 & 0 & 0 & 0 \end{bmatrix} . \tag{18}$$

The components of $\mathbf{X}$ can be conveniently converted to center $[Cx\ Cy]$, radii $[Rx\ Ry]$ and tilt α of the ellipse (the latter indicating which axes the ellipse is scaled along); once these quantities are known, the points can be mapped to a circle using the following transformation:

$$\mathbf{m}_i^c = R_z(\alpha) \begin{bmatrix} r/Rx & 0 & 0 \\ 0 & r/Ry & 0 \\ 0 & 0 & 1 \end{bmatrix} R_z^T(\alpha) \left(\mathbf{m}_i^h - \begin{bmatrix} Cx \\ Cy \\ 0 \end{bmatrix} \right) , \tag{19}$$

where $R_z(\alpha)$ denotes a rotation about the z-axis of an angle α.

The obtained circle has a radius of r and zero x and y coordinates of its center. The offset on the z-axis can be computed as the difference between the z coordinate of the points $\mathbf{m}_i^h$ and H_z^I (Fig. 5d).

4. NECF

4.1. NECF classic formulation

The attitude estimation filter adopted is the explicit complementary filter proposed by Mahony et al., whose stability and convergence has been proved in 2008 [13]. This section offers a brief review of the classic formulation of the filter; then, the modifications applied to the original structure are explained.

The NECF computes an estimate of the attitude of the IMU at each iteration; the basic idea is to integrate the angular rate changes measured by the gyroscope, correcting the estimate with accelerometer and magnetometer readings. The convergence of the algorithm has been proven if measurements of at least two fixed **nonparallel** directions in the inertial frame are measurable with respect to the sensor frame. This condition is usually satisfied by commercial IMUs that are equipped with a 3-axis gyroscope, a 3-axis accelerometer and a 3-axis magnetometer. In particular, accelerometer readings give an estimate of the direction of gravitational acceleration (assuming that the sensor proper acceleration is negligible, as it is usually in the field of underwater robotics), and thus they are used to correct roll and pitch angles; magnetometers measure the direction of Earth's magnetic field, and thus act on the yaw value. Furthermore, an estimate of the bias of the gyroscope is computed.

The filter is a dynamical system governed by the following equations [13]:

$$\dot{\hat{R}} = \hat{R} \left(\left(\boldsymbol{\omega}_m^B - \hat{\mathbf{b}}_g \right)_\times + k_P \left(\boldsymbol{\omega}_{mes} \right)_\times \right), \quad \hat{R}(0) = \hat{R}_0 \tag{20}$$

$$\dot{\hat{\mathbf{b}}}_g = -k_I \boldsymbol{\omega}_{mes} \tag{21}$$

$$\boldsymbol{\omega}_{mes} = \sum_{i=1}^n k_i \mathbf{v}_i \times \hat{\mathbf{v}}_i, \quad k_i \geq 0, \quad i = 1, \cdots, n . \tag{22}$$

Concerning the notation, $\hat{\cdot}$ indicates an estimated value, $\hat{R}$ is an estimate of the rotation matrix which defines the attitude of the sensor (being $\hat{R}_0$ the initial estimate), k_P and k_I are tunable gains, and $(\mathbf{a})_\times$ is the operator that builds a skew-symmetric matrix from vector $\mathbf{a}$:

$$(\mathbf{a})_\times = \begin{bmatrix} 0 & -a_3 & a_2 \\ a_3 & 0 & -a_1 \\ -a_2 & a_1 & 0 \end{bmatrix} . \tag{23}$$

The term $\boldsymbol{\omega}_{mes}$ requires detailed explanation: it is indeed the correction term built upon accelerometer and magnetometer measurements.

6

Let $\mathbf{v}_{0,i}$, with $i = 1, \cdots, n$, be a set of known inertial directions, and let

$$\mathbf{v}_i = R^T \mathbf{v}_{0,i} + \boldsymbol{\mu}_i \qquad (24)$$

and

$$\hat{\mathbf{v}}_i = \hat{R}^T \mathbf{v}_{0,i} \qquad (25)$$

denote, respectively, its measurement in the sensor frame (affected by noise $\boldsymbol{\mu}_i$) and its estimate (computed using the estimated rotation matrix $\hat{R}$); the term $\boldsymbol{\omega}_{mes}$ is the weighted sum of the misalignment between the measured directions and their estimates computed using the output of the filter. In particular, in the considered case the direction of the vertical axis (measured by the accelerometer) and the direction of the magnetic field (read by the magnetometer) are taken into account; the weights k_i are chosen according to the relative confidence in each measurement $\mathbf{v}_i$.

Let $\tilde{R} = \hat{R}^T R$ and $\tilde{\mathbf{b}}_g = \mathbf{b}_g - \hat{\mathbf{b}}_g$ denote, respectively, the orientation and gyro bias errors; then, for $n > 1$, Mahony et al. [13] have proven through the use of Lyapunov theory that $(I, \mathbf{0})$ **is a locally exponentially stable equilibrium point of the error dynamics** $(\tilde{R}, \tilde{\mathbf{b}}_g)$.

4.2. Design changes

When applying the NECF in its classical formulation (20)-(22) to measurements coming from an IMU used for the estimation of the attitude of an underwater vehicle, several issues arise. Hence, some design changes have been applied to the original formulation of the filter in order to better adapt it to the considered application. This section illustrates and justifies in details each applied modification; an experimental test campaign was conducted to verify the properties and effectiveness of the proposed method.

4.2.1. Filter on accelerometer measurements

Through suitable preliminary tests executed out of the water, it has been experimentally observed that oscillating movements of the IMU on the horizontal plane cause unwanted variations of roll and pitch angles extracted from the output rotation matrix of the filter; this is because sudden horizontal movements are interpreted by the accelerometer as deviations of the vertical direction, thus affecting the computation of the rotation matrix. This phenomenon has to be identified and corrected in real time, in order to produce accurate attitude estimates. To reduce the amplitude of these variations and to obtain a smoother profile for such angles, accelerometer measurements have been filtered. Several filter orders and cutoff frequencies have been tested; a second order transfer function has been chosen, constituting a suitable trade-off between the accuracy of the roll and pitch estimates and the readiness of the NECF. The adopted filter has the following form:

$$\mathbf{a}_f = F(z)\mathbf{a}_m^B \ . \qquad (26)$$

$F(z)$ is obtained by discretizing the unit gain second order filter

$$F(s) = \frac{\omega^2}{(s + \omega)^2} \qquad (27)$$

with the bilinear (Tustin) transform:

$$F(z) = F(s)\big|_{s = \frac{2}{T}\frac{z-1}{z+1}} \ , \qquad (28)$$

where T is the time between two subsequent iterations of the filter (which can be considered constant). The resulting discrete filter realizes the following recurrence relation:

$$\mathbf{a}_f(k) = \frac{1}{\epsilon}\bigg(\beta\mathbf{a}_m^B(k) + \gamma\mathbf{a}_m^B(k-1) + \delta\mathbf{a}_m^B(k-2) +$$

$$-\nu\mathbf{a}_f(k-1) - \rho\mathbf{a}_f(k-2)\bigg) \ , \qquad (29)$$

for given coefficients $\beta, \gamma, \delta, \epsilon, \nu, \rho$ which depends on T and ω.

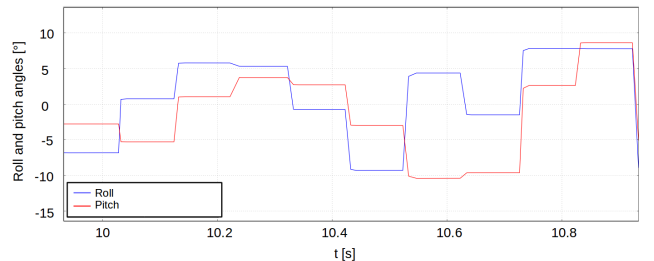Note that, since only the direction of the acceleration

Figure 7: Roll and pitch angles (degrees) without acceleration filter.
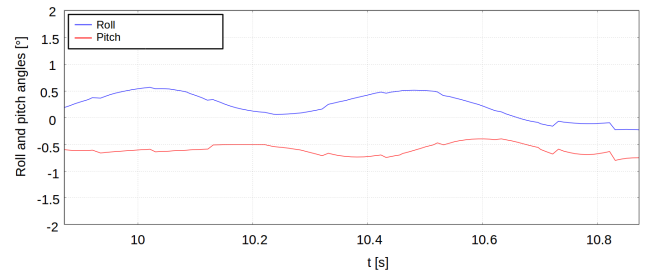

Figure 8: Roll and pitch angles (degrees) with acceleration filter.

vector is important, vector $\mathbf{a}_m^B$ is normalized before being filtered by $F(z)$; the same operation is executed on $\mathbf{a}_f$ before its use in $\boldsymbol{\omega}_{mes}$ (the notation is not changed for the ease of reading).

The effect of the filter is visible comparing Figure 7 and Figure 8, obtained using the visualization tool *rqt_plot* of the software ROS [32]: each figure shows the roll and pitch angles, expressed in degrees, extracted from the rotation matrix $\hat{R}$ during oscillating movements of the IMU on a horizontal plane. It is easy to note the huge improvement achieved with the use of a filter on accelerometer readings: in the second case, oscillations are very small (less than one degree), and a decrease of the error of an order of magnitude with respect to the case when no filter is used is obtained.

4.2.2. Known directions choice

The classic formulation of the NECF filter relies on at least two known **nonparallel** inertial directions measured in the sensor frame. The most natural choice, considering the available commercial sensors, is to use the local measurements of the gravitational acceleration and of the Earth's magnetic field. These quantities are used in the correction term $\boldsymbol{\omega}_{mes}$, where they are compared with the estimates of the chosen directions to generate an error term.

The proposed modification consists in choosing only the component of the measured magnetic field which is orthogonal to the acceleration direction instead of the complete magnetometer measurement (a similar approach can be found in [5], [6]). This choice is justified because of the following considerations: first of all, it is worth to note that, since the vehicle proper acceleration is usually negligible compared to gravity, and rotations along x-axis and y-axis are constrained, the plane orthogonal to acceleration approximately coincides with the horizontal plane all the time (i.e. the accelerometer measurements give the direction of the inertial vertical direction $\mathbf{z}^I$); in addition, accelerometer readings are more reliable than magnetometer measurements, mainly because the former are not affected by external error sources as the latter are. Thus, by including the vertical component of the measured magnetic field, even in the absence of external magnetic disturbances, no further benefits are gained compared to using only the information carried by the acceleration estimate.

Hence, after applying the proper correction using the parameters determined during the calibration phase, the projection of magnetometer measurements onto the plane orthogonal to acceleration is computed:

$$\mathbf{m}^c_{\perp} = \mathbf{m}^c - \left((\mathbf{a}_f)^T \mathbf{m}^c \right) \mathbf{a}_f . \qquad (30)$$

Thanks to the previous observations, $\mathbf{m}^c_{\perp}$ (once expressed in the inertial frame) is a vector pointing towards North magnetic pole thus, after normalization, in $\boldsymbol{\omega}_{mes}$ it is compared with the estimate of the inertial north direction

$$\hat{\mathbf{x}}^I = \hat{R}^T \begin{bmatrix} 1 \\ 0 \\ 0 \end{bmatrix} . \qquad (31)$$

4.2.3. Time varying gains

In Equation (22), the gains k_i of the correction term are constant and prefixed. However, during the normal functioning of the filter, it may happen that measurements provided by accelerometers or magnetometers are affected by unpredictable transitory errors. These situations should be detected and the gains should be scaled according to the real time reliability of each measurement.

In the considered case study, gains k_i are constant only during the initialization of the filter; then, they are eventually scaled over time (never exceeding the initial value), in order to discard unreliable measurements in real time. The

procedure is different for the acceleration and the magnetic field readings.

Acceleration gain. The acceleration gain k_1 is linearly decreased with the acceleration magnitude if high acceleration occurs, in order to avoid that sudden accelerations along some directions generate a wrong contribute to the correction term of the filter (cfr. 4.2.1). During the initialization, k_1 is fixed at the initial value determined through a preliminary tuning process, and the average value $\bar{a}$ of the magnitude of acceleration measurements is computed to be used as a reference term. Then, k_1 is set according to the relative distance between the norm of the acceleration measurement and $\bar{a}$:

$$D_a = \left| \frac{||\mathbf{a}^B_m|| - \bar{a}}{\bar{a}} \right| . \qquad (32)$$

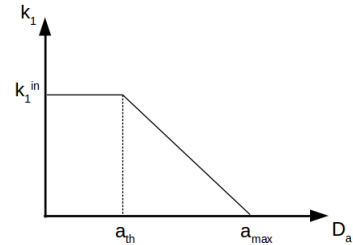Referring to Figure 9: a_{th} represents the threshold value

Figure 9: Computation of gain k_1.

which, if exceeded, causes the decrease of the gain until the maximum value a_{max} is reached, at which k_1 is set to zero.

Let k_1^{in} denote the initial (constant) gain; if $a_{th} < D_a < a_{max}$, k_1 is determined according to:

$$k_1 = k_1^{in} \left(-\frac{1}{a_{max} - a_{th}} D_a + \left(1 + \frac{a_{th}}{a_{max} - a_{th}} \right) \right) . \qquad (33)$$

For $D_a < a_{th} \rightarrow k_1 = k_1^{in}$ and for $D_a > a_{max} \rightarrow k_1 = 0$.

Magnetic field gain. As stated in Section 3, even using a proper calibration technique, only disturbances which rotate with the sensor can be compensated. External metal objects are inevitably a source of magnetic disturbance that affects the yaw estimate. Their presence is not uncommon, especially in the field of underwater robotics:for example, many AUVs are used for inspection tasks of modern wrecks, mainly composed of metal parts and debris.

Since these disturbances cannot be corrected, the only possible countermeasure is to readily detect corrupted readings and to avoid the use of the magnetometer measurements in such situations, relying only on gyroscope integration for the yaw estimate.

The gain k_2 associated with the magnetometer readings is changed according to a different strategy with respect to the accelerometer gain k_1. It is indeed likely that

external disturbances modify the direction of the magnetic field without sensibly varying its magnitude; hence, a magnitude-related law would prove unreliable, leading to the use of wrong information for correction purposes. The idea is then to scale down k_2 if two particular angular constraints are violated. If accurate gyroscope data are available, on a brief period of time the error obtained integrating the angular velocity is lower than the error generated by considering the corrupted magnetic measurements.

The first angle to be checked is the angle between the projection of the corrected measurement onto the plane orthogonal to the acceleration vector (which can be assumed to be the horizontal plane, see Sec. 4.2.2) and the estimate of the x-axis:

$$\alpha^1_{check} = cos^{-1}\left((\mathbf{m}^c_\perp)^T \hat{\mathbf{x}}^I\right) . \tag{34}$$

In ideal conditions, the magnitude of α^1_{check} is zero (or, since sensors are affected by measurement noise, it has zero mean value). If a source of magnetic disturbance gets close to the sensor, the change in the magnetometer readings cause the estimated rotation $\hat{R}$ to vary. However, since the dynamics of the magnetometer are much faster than the filter, if the disturbance approaches the sensor sufficiently rapidly a deviation of $\mathbf{m}^c_\perp$ is registered before a relevant change in $\hat{R}$ may occur, thus causing the increase of α^1_{check}.

Nevertheless, the use of α^1_{check} only to verify the correctness of the magnetometer readings has a drawback: if the magnetic disturbance approaches the sensor very slowly, the velocity of the drift of the sensor reading may match the dynamics of the filter: in this case, a slow but continuous change in the yaw angle is registered, with α^1_{check} remaining close to zero even if a disturbance is present.

A second control angle α^2_{check} is thus introduced to overcome this problem. The choice of α^2_{check} is based on the following consideration: in a given geographical location the Earth's magnetic field can be considered constant: i.e. the angle between $\mathbf{H}^I$ and the vertical direction $\mathbf{z}^I = [0\ 0\ 1]^T$ is constant. The same angle must be measured between the same vectors rotated in the body frame. Mathematically, this equality is expressed by the following equation:

$$\left(\mathbf{z}^I\right)^T \mathbf{H}^I = (\mathbf{a}_f)^T \mathbf{m}^c , \tag{35}$$

where the body frame vertical direction is given by the filtered accelerometer measurement.

Hence, α^2_{check} measures the angular distance between the angle $(\mathbf{a}_f)^T \mathbf{m}^c$ obtained at each iteration and the corresponding value $\left(\mathbf{z}^I\right)^T \mathbf{H}^I$:

$$\alpha^2_{check} = \left|\left|cos^{-1}\left((\mathbf{a}_f)^T \mathbf{m}^c\right) - cos^{-1}\left(\left(\mathbf{z}^I\right)^T \mathbf{H}^I\right)\right|\right| . \tag{36}$$

The magnitude of α^2_{check} is independent from the speed at which a magnetic disturbance is applied.

Note that, in Eq. (35) and Eq. (36), only the directions of the involved vectors are considered.

Two threshold values α^1_{th} and α^2_{th} are then set; if either one is reached, k_2 is forced to zero in a finite number of iterations. If both angles fall below the threshold values, k_2 is increased back to the initial value. The decrease is much faster than the increase.

Let k^u and k^d denote increase and decrease counters, and let k^u_{max} and k^d_{max} be the number of iterations allowed for the variation of the gain k_2. If k^{in}_2 is the initial value for k_2, then Algorithm 1 illustrates how the magnetometer gain is computed.

Data: k^{in}_2, k^u_{max}, k^d_{max}
Result: gain k_2
if $\alpha^1_{check} > \alpha^1_{th}$ *or* $\alpha^2_{check} > \alpha^2_{th}$ **then**
$\quad$ $k_2 = k^{in}_2\left(1 - k^d/k^d_{max}\right)$;
$\quad$ $k_2 \geq 0$;
$\quad$ $k^d + +$;
$\quad$ $k^u = 0$;
else
$\quad$ $k_2 = k_2 + \left(k^{in}_2 - k_2\right)(k^u/k^u_{max})$;
$\quad$ $k_2 \leq k^{in}_2$;
$\quad$ $k^u + +$;
$\quad$ $k^d = 0$;
end

Algorithm 1: k_2 computation.

It is possible for both angles to become greater than the threshold values even if no magnetic disturbances are present; this can occur if large accelerations arise (not likely to happen in the field of underwater robotics) or during motion transients. However, the effect is only temporary and α^1_{check}, α^2_{check} fall again below the threshold in a short amount of time. This solution may appear quite conservative; nonetheless, if a precise gyroscope is available, it is indeed better to discard good magnetometer readings than running the risk of including corrupted magnetic measurements, thus compromising the accuracy of the yaw estimate.

Generally, the calibration phase should be performed only at the beginning of a navigation mission; however, in unfavorable conditions (e.g. if the calibration algorithm has been executed in a **magnetically disturbed environment**) the control angles may remain greater than the threshold values, hence excluding the magnetometer from the filter recursions for a long time. In such cases, it may be useful to temporarily stop the mission and to perform a new calibration.

In conclusion, in the considered case study $\boldsymbol{\omega}_{mes}$ has the following form:

$$\boldsymbol{\omega}_{mes} = k_1 \mathbf{a}_f \times \hat{R}\mathbf{z}^I + k_2 \mathbf{m}^c_\perp \times \hat{R}\mathbf{x}^I . \tag{37}$$

4.2.4. FOG integration

Most commercial IMUs offer integrated algorithms that estimate attitude on the basis of raw measured data coming from the sensors they are equipped with. The use of a

stand-alone attitude estimation filter yields the possibility of using data that come from external (i.e. not built-in in the IMU) sensors in order to increase the accuracy of the obtained estimate. This is extremely useful in low cost applications, where cheaper MEMS sensors can be used together with more precise sensors. In the considered case, a single-axis Fibre Optic Gyroscope (FOG), an accurate and reliable sensor based on the Sagnac effect, has been mounted with its sensitive axis parallel to the IMU's gyroscope z-axis. Its measurement completely substitutes the axis angular rate change read by the IMU gyroscope.

The reason behind this choice is the following: the magnetometer related contribution in $\boldsymbol{\omega}_{mes}$ has the purpose of obtaining an accurate estimation of the yaw angle. In the case of magnetic disturbances the gain k_2 is set to zero, and the yaw estimate is obtained by raw integration of the angular velocity. Since the IMU gyroscope possesses a much higher bias then the FOG, relevant yaw drift is present even if the sensor is not moving. Such a precise device allows to reach a high level of accuracy; through its use, the risk of unacceptable growth of the integration error when the magnetometer is not employed is avoided. However, the use of a FOG has a drawback: even if the component is not rotating, the device senses Earth's angular velocity, thus producing a nonzero output of up to 15° per hour. **If three high-grade gyroscopes are available (one for each axis), the Earth's rotation sensed in the body frame can be exploited within the estimation process (e.g. [22]). However, this solution is very expensive; in this context, since only one high-precision gyroscope is available, the effect of Earth's rotation is considered a disturbance to be rejected. Indeed, its contribute on the FOG output can be compensated exploiting the knowledge of the latitude at which the sensor is operating and the information regarding the roll and pitch angles.**
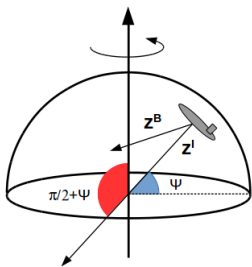

Figure 10: FOG correction term computation.

Referring to Figure 10: it is assumed that the sensor is operating in the Earth's northern hemisphere; however, the compensation procedure is conceptually the same on the whole planet surface. Let $\boldsymbol{\omega}_E$ denote Earth's angular velocity; its magnitude, expressed in radians per second, is then

$$\omega_E = ||\boldsymbol{\omega}_E|| \cong 7.2921 \cdot 10^{-5} \; . \qquad (38)$$

The latitude Ψ is supposed to be known. The compensation algorithm is composed of two steps: at first, $\boldsymbol{\omega}_E$ is projected onto the inertial z-axis; then, on the basis of roll and pitch values, the magnitude of the resulting vector is projected onto the body z-axis $\mathbf{z}^B = R^T \mathbf{z}^I$ and subtracted from the sensor readings.

The magnitude of Earth's angular velocity projected onto $\mathbf{z}^I$ is given by

$$\omega_E^\perp = \omega_E \; cos(\pi/2 + \Psi) \; ; \qquad (39)$$

in order to find the desired correction term this quantity has to be multiplied by the result of the dot product $\left(\mathbf{z}^I\right)^T \mathbf{z}^B$. $\mathbf{z}^B$ can be computed by pre-multiplying $\mathbf{z}^I$ by the composition of the roll (ϕ) and the pitch (θ) rotation matrices:

$$\mathbf{z}^B = (R_{x,y}(\phi, \theta))^T \mathbf{z}^I = (R_y(\theta) R_x(\phi))^T \mathbf{z}^I \; . \qquad (40)$$

It is easy to verify that the result of the dot product $\left(\mathbf{z}^I\right)^T \mathbf{z}^B$ is

$$\left(\mathbf{z}^I\right)^T \mathbf{z}^B = R_{x,y}(3,3) = cos(\phi)cos(\theta) \; . \qquad (41)$$

In conclusion, the corrected FOG measurement is given by:

$$\omega_{FOG}^c = \omega_{FOG} - \omega_E^\perp cos(\phi)cos(\theta) \; , \qquad (42)$$

where ω_{FOG} indicates the uncompensated reading.

After the correction has been applied, highly accurate measurements can be obtained: in the considered case study, mere integration over time of the compensated measurement while the device was held still showed an angle drift of about 2° per hour.

5. Test results

The performances of the proposed filter have been tested on the Typhoon AUV [17], [19], developed and built by the MDM Lab of the University of Florence (visible in Figure 11 during a sea trial) in the framework of the THESAURUS[1] and the ARROWS[2] [33] projects. In addition, preliminary tests have been executed to validate the magnetometer calibration algorithm introduced in Sec. 3.

The vehicle is equipped with a Xsens Technologies MTi-G-700 INS and a single-axis KVH DSP-1750 Fiber Optic Gyro mounted with its sensitive axis pointing down (aligned with the IMU z-axis) (Figure 12). Mounting both sensors on a rigid panel allowed to obtain a very limited misalignment error between the FOG axis and the IMU z-axis, which did not cause particular issues during the tests performed. Nonetheless, a pre-test calibration procedure could be used to compute a constant correction matrix should relevant misalignment occur.

---

[1]THESAURUS project: *www.thesaurus.isti.cnr.it*
[2]ARROWS project: *www.arrowsproject.eu*

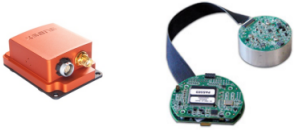Figure 11: Tiphoon AUV at sea.

Figure 12: Sensors used to estimate the attitude of the Typhoon AUV.

Xsens MTi is equipped with a 3-axis gyroscope, a 3-axis magnetometer and a 3-axis accelerometer; in addition, it ships with its own magnetometer calibration procedure and attitude estimation algorithm, while the DSP-1750 FOG outputs raw angular velocity data. The noise specifications of the considered sensors, extracted from the corresponding datasheets, are reported in Table 1.

Sensor noise specifications			
Xsens IMU			
	Gyroscope	**Accelerometer**	**Magnetometer**
Noise density	$0.01°/s/\sqrt{Hz}$	$80\ \mu g/\sqrt{Hz}$	$200\ \mu G/\sqrt{Hz}$
KVH FOG			
Angle Random Walk			$\leq 0.05°/\sqrt{hr}$

Table 1: Sensor noise specifications.

To validate the magnetometer calibration algorithm and to evaluate its performances, two suitable calibration tests have been executed: the first one has been performed in a disturbance-free environment, while during the second test a metal object has intentionally been placed close to the sensor during its rotation (with the sensor and the disturbance source rotating together). The magnetometer readings during both tests have been acquired before and after the calibration procedure.

Figures 13-18 report the obtained results: for both tests, the 3D measurement locus is shown; in addition, the rotated measurements $\mathbf{m}^h$ are reported (along with the center and the radii directions of the best fitting ellipses); finally, Figures 15, 18 show the calibrated magnetic field measurements.

In the first test, the measurement locus is close to the theoretical circle, the only disturbances being those due to
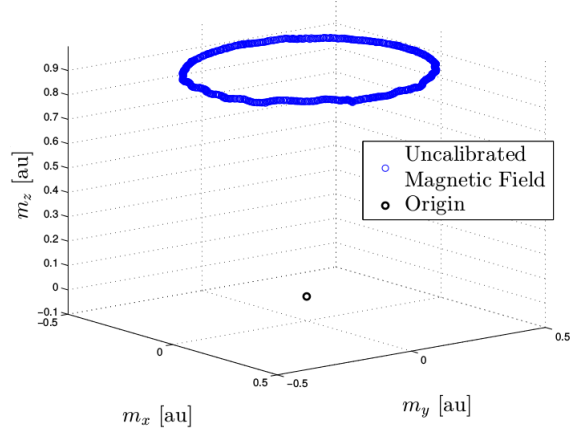

Figure 13: Disturbance-free calibration test: 3D sensor readings locus.
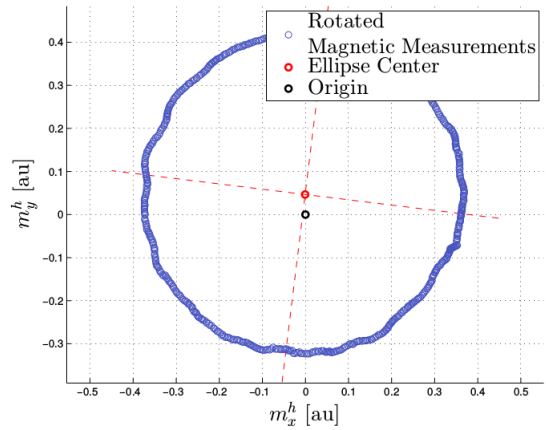

Figure 14: Disturbance-free calibration test: rotated magnetic field measurements.

electronics close to the sensor housing; in this case, when no relevant magnetic disturbance is present, no significant changes are applied to the direction of the magnetometer readings. On the contrary, when a metal object is brought close to the sensor during the calibration turn, the tilt and the shift from the origin of the resulting compass readings locus are relevant (Figure 16 shows a three-dimensional view). Nonetheless, after the proposed calibration algorithm has been applied, the measurements are correctly mapped back to the theoretical circle (Figure 18). Table

	Test 1	**Test 2**
Center coordinates	Cx:-0.000749358 Cy:0.0466289	Cx:-0,109029 Cy:0.0104137
Radii length	Rx:0.377051 Ry:0.367223	Rx:0.519005 Ry:0.440094

Table 2: Measurement ellipse characteristics.

2 reports the characteristic parameters (coordinates of the center and length of the radii) of the ellipses obtained after projecting the measurements on the plane of minimal
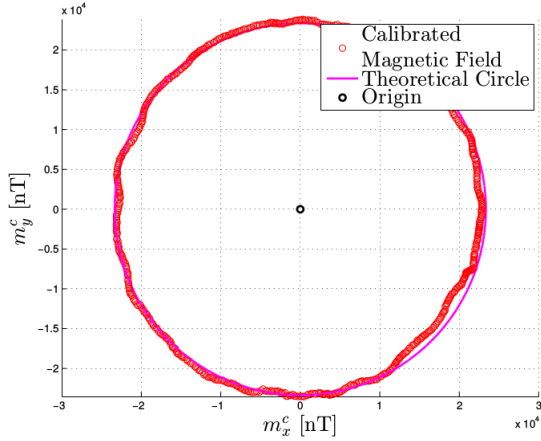
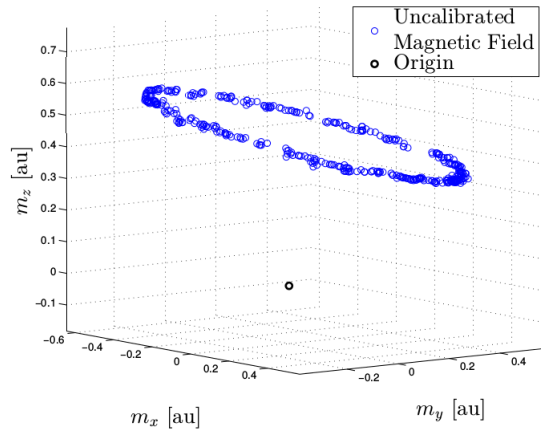Figure 15: Disturbance-free calibration test: calibrated magnetic field.

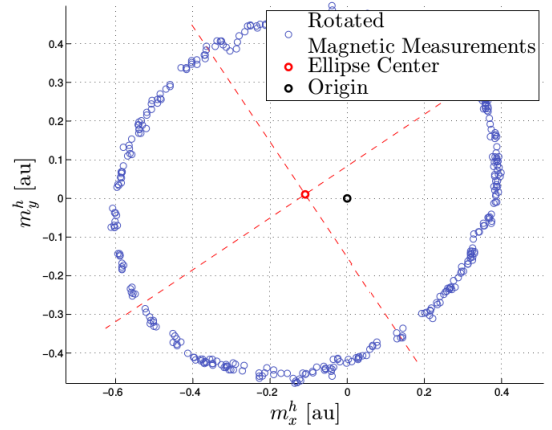Figure 16: Magnetically perturbed calibration test: 3D sensor readings locus.

Figure 17: Magnetically perturbed calibration test: rotated magnetic field measurements.
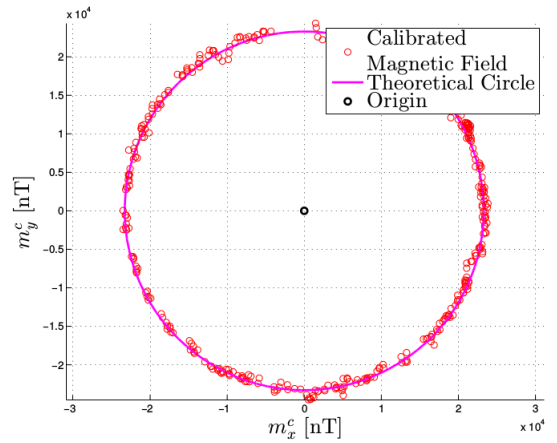
Figure 18: Magnetically perturbed calibration test: calibrated magnetic field.

distance and aligning the latter with the horizontal plane (Figures 5a-5c). Such ellipses are those shown in Figures 14, 17.

For what concerns the first test, it is clearly visible that a minor Hard Iron disturbance is present (as stated before, this effect is likely due to the other components of the vehicle which are mounted close to the sensor), while the radii of the ellipse are very close (no Soft Iron effect). On the other side, the parameters obtained during the second calibration test indicate relevant shift and tilt (consistent with Figures 16, 17), evidence of significant Hard and Soft Iron disturbances.

In both cases, the proposed calibration algorithm is capable of compensating such disturbances, mapping back the magnetometer measurements to the correct locus, as shown in Figures 15, 18.

When comparing Figures 13-18, it is worth to note:

- the magnetic field measurements are given by the sensors in **arbitrary units (au)**, while the proposed calibration algorithm converts them to nT; this conversion is irrelevant to the estimation filter, since only

the direction of the magnetic field vector is considered;

- the data acquired during the first test are uniformly distributed across the whole circle, while the data obtained during the second test are more sparse. This is due to different environmental conditions: two threshold values for the roll and the pitch angles have been set in order to discard measurements which fall beyond such values; the aim is to consider only readings which are sufficiently close to the horizontal plane. Hence, adverse environmental conditions (such as waves and currents) may lead to increased oscillations of the vehicle, with a consequent discard of several readings (since the threshold values are intentionally strict); however, if too few measurements are available (not enough to give reliable results), the calibration procedure may require additional turns to be completed.

After the validation of the magnetometer calibration algorithm, suitable attitude estimation tests have been executed; these tests aim at comparing the roll, pitch and yaw estimates given by the IMU internal algorithm with

the corresponding angles extracted from the output rotation matrix of the proposed filter presented in the previous section. The first test consists in calibrating the sensor and completing a whole turn about the sensor z-axis. Since the IMU is sold with a proprietary magnetometer calibration software, both the proprietary and the proposed compass calibration algorithms have been executed: the calibration parameters obtained with the proprietary software (which are unknown to the authors, as well as the calibration algorithm) have been used within the IMU internal estimation filter, while the measurements corrected by exploiting the proposed calibration procedure have been used within the NECF.

A first turn about the vertical axis is performed, and the data are used to run the calibration algorithm explained in Sec. 3; then, a second turn is executed to evaluate the performances of the filter. Let

$$\Phi_{filter} = [\phi_{filter} \ \theta_{filter} \ \psi_{filter}]^T$$

denote roll, pitch and yaw angles extracted from the output of the proposed filter $\hat{R}$, and

$$\Phi_{Xsens} = [\phi_{Xsens} \ \theta_{Xsens} \ \psi_{Xsens}]^T$$

be the corresponding angles given by the Xsens internal algorithm.
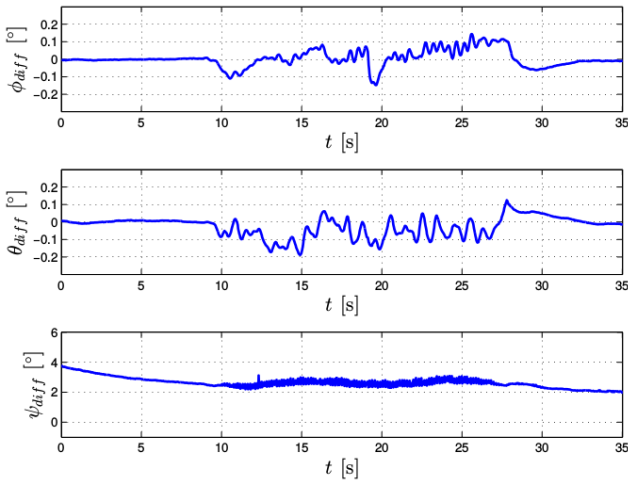

Figure 19: Φ_{diff} obtained during the first test.

Figure 19 reports the three components of the vector $\Phi_{diff} = \Phi_{filter} - \Phi_{Xsens} = [\phi_{diff} \ \theta_{diff} \ \psi_{diff}]^T$ obtained during the first test. It is clearly visible that the roll and the pitch differences are very small, not exceeding 0.2°. The yaw difference is close to a value of more than 3° almost all the time. This is consistent with the difference between geographic North (which yields zero yaw for the Xsens algorithm) and magnetic North: in the proposed filter, the contribute to the correction term ω_{mes} given by the magnetometer is computed as the (weighted) angular difference between the corrected magnetic field readings projected onto the horizontal plane and the estimate of

the vector $\mathbf{x}^I = [1 \ 0 \ 0]^T$; hence, the condition of zero error is obtained when the y component of the magnetic field is null (i.e. when the sensor is pointing towards magnetic North). **The Xsens sensor instead is equipped with a GPS receiver, thus it compensates for magnetic declination exploiting GPS data and computes the yaw estimate with respect to true North.** This is further supported by the fact that, at the geographical location where the tests have taken place (i.e. Tuscany, Italy), the difference between the geographic and the magnetic North is about 3°.
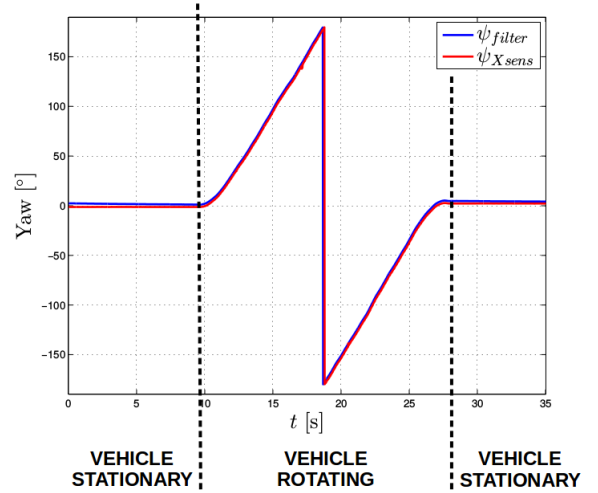

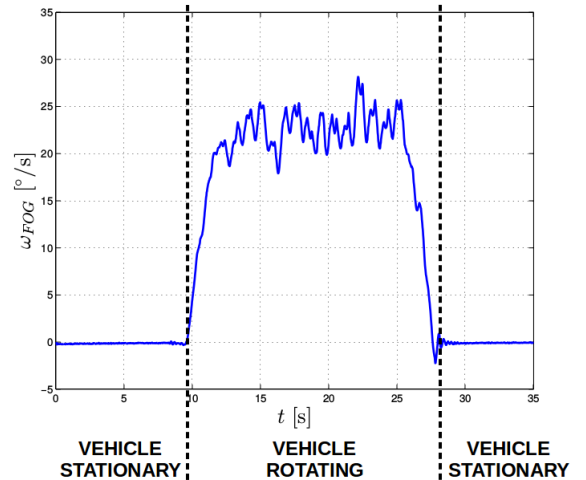Figure 20: Yaw values obtained during the first test.

Figure 21: FOG signal obtained during the first test.

The yaw angle values for the considered algorithms are visible in Figure 20, highlighting how they almost overlap during the entire test. In addition, Figure 21 shows the FOG angular rate change measured during the test: such signal is used as a reliable indication of the actual rotation of the vehicle, exploited to show how the yaw estimate computed by the proposed filter corresponds to the real orientation of the AUV.
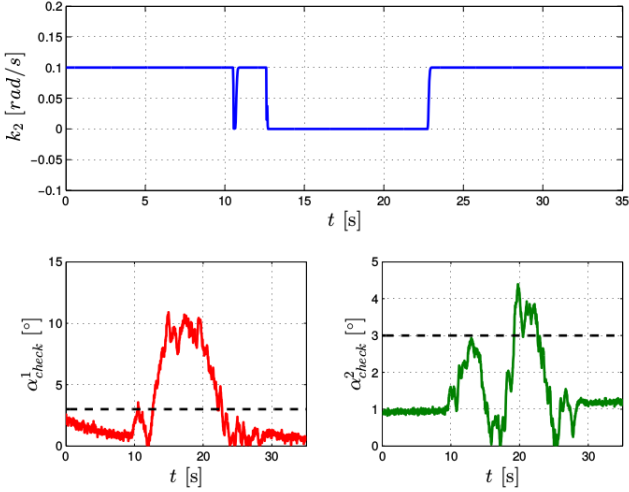
13

Figure 22: k_2 and control angles values obtained during the first test.

Figure 23: Φ_{diff} obtained during the second test.

Regarding the behavior of the proposed filter, Figure 22 shows the variation of the gain k_2 during the test, along with the two control angles α^1_{check} and α^2_{check}; since large accelerations do not occur, gain k_1 remains fixed at its maximum value and is not reported. The horizontal dashed black lines indicate the threshold values, set at 3° for both angles.

As mentioned in Sec. 4.2.3, it is shown how the gain is reduced to zero even if no magnetic disturbances are present: comparing Figures 20 and 22 it is visible that the yaw estimate relies only on the integration of the FOG for about half turn; however, since such device is very precise (with an even increased accuracy after the correction of Earth's angular velocity bias) the estimate remains very accurate. Hence, in the absence of magnetic disturbances, it has been shown that the two attitude estimation algorithms are consistent and both offer accurate estimates.

The second test performed shows how the Xsens algorithm may run into problems when magnetic disturbances (be them magnets or ferromagnetic objects) get close to the sensor, causing the output to diverge from the correct attitude. The presented filter, instead, guarantees a correct estimate even in the presence of disturbances.

This test is composed of the following steps: without performing a new magnetometer calibration, the vehicle is at first kept still until convergence of the filter, then a piece of metal is placed close to the sensor; after a given amount of time, a clockwise rotation of about 40° is performed, and the metal object is finally removed.

Similarly to the previous test, Figure 23 reports the difference between the outputs of the two algorithms; while ϕ_{filter} and θ_{filter} remain close to their counterparts, the same does not apply for the yaw estimates, which exhibit a relevant difference.

See Figure 24 and Figure 26 for a better understanding: it is clearly visible that, when the piece of metal is brought close to the sensor (at about 17s), α^1_{check} and α^2_{check} as-
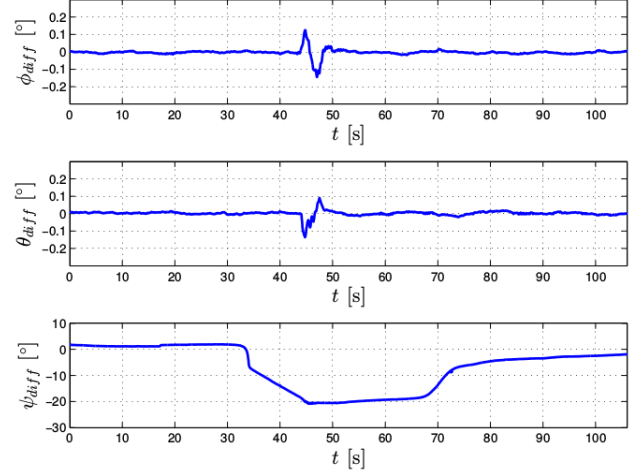
sume a very high value and the gain k_2 is promptly reduced to zero. The Xsens algorithm, however, does not recognize the disturbance, causing a relevant deviation of the yaw estimate (compare the FOG signal shown in Figure 25) even if the vehicle is kept still (starting from 32s). When the disturbance source is removed after the rotation (50s), the control angle values both fall below the threshold and the gain k_2 is set to its initial value again. By observing Figure 24 it is easy to understand the behavior of the filter: when k_2 is set to zero, the yaw estimate is computed integrating the FOG readings. While the vehicle is not rotating, such angle exhibits a drift due to the integration of the gyroscope bias; however, due to the precision of the device, the deviation in the short term is negligible. This is further supported by the fact that, after the gain is incremented again, the correction applied by the magnetometer does not affect the current estimate much. This is not the case of the internal algorithm of the Xsens: when the disturbance is added, a significant yaw drift is registered. Even if the IMU gyroscope integration is almost equal to the rotation imposed, when the disturbance is removed the final estimate is affected by the wrong integration initial value. Hence, as seen in Figure 24, the algorithm slowly converges to the correct estimate given by the proposed filter (with the angular difference due to magnetic declination accounted for).

To further evaluate the performances of the proposed filter, several additional estimation tests have been executed, composed of the following steps:

- Magnetometer calibration: both the proprietary and the proposed calibration algorithms are executed, and the obtained corrections are employed within the respective filters;

- Filter initialization: the filters are initialized while the vehicle is not moving;

- Addition of a magnetic disturbance: a metal object is attached close to the sensor;
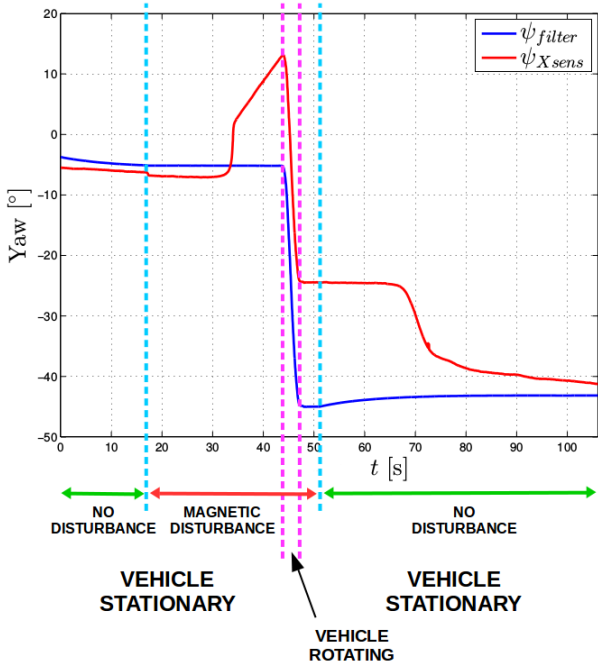
14

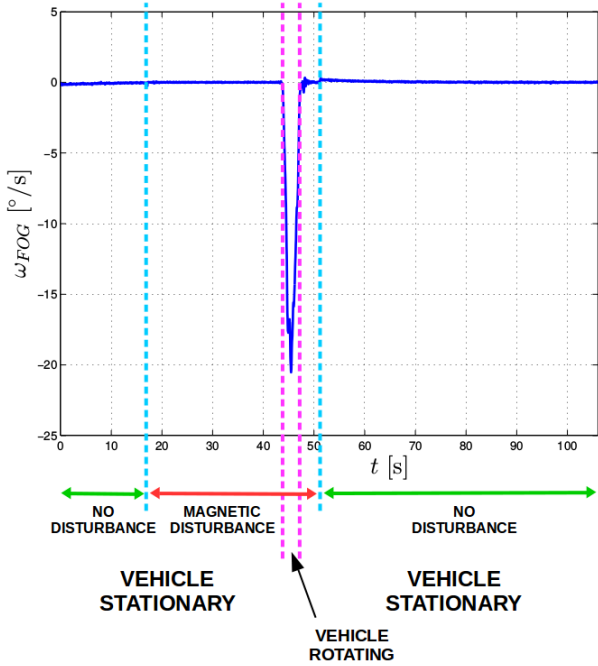Figure 24: Yaw values obtained during the second test.

Figure 25: FOG signal obtained during the second test.

- Rotation: the AUV is rotated (together with the disturbance source);

- Disturbance removal;

- Inverse rotation: the vehicle is rotated back.

The obtained results are similar for all the tests performed; those presented in the following refer to a specific test, assumed as case study.
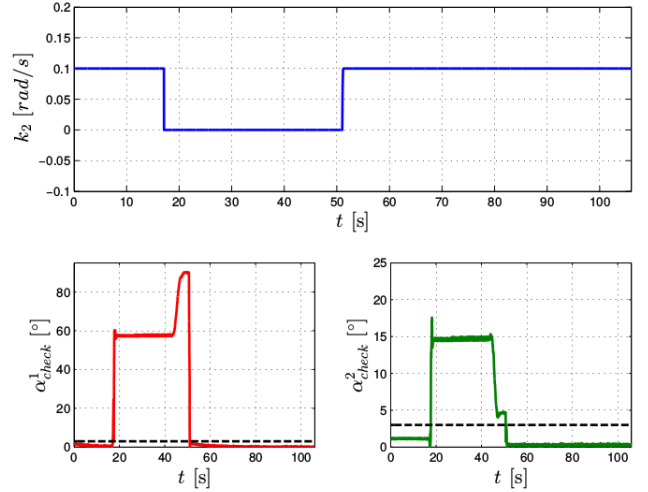

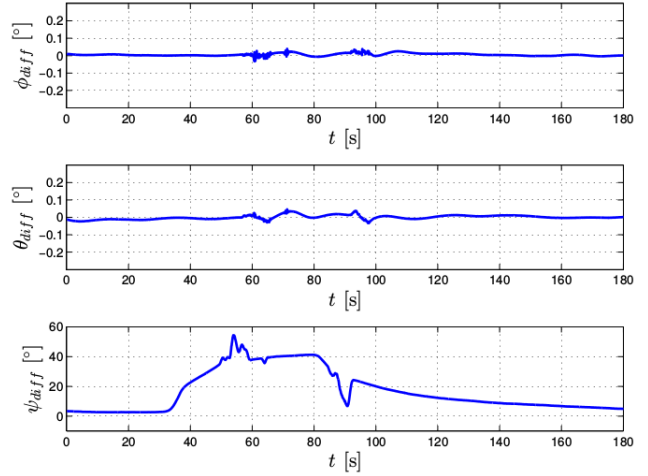Figure 26: k_2 and control angles values obtained during the second test.

Figure 27: Φ_{diff} obtained during the third test.

As for the previous test, significant yaw difference is present after the magnetic disturbance has been applied, while ϕ_{diff} and θ_{diff} remain close to zero during the whole test (Figure 27); the Xsens filter, exploiting the corrupted magnetic field readings, outputs a variation in the attitude of the AUV even when the latter is not moving (compare the FOG measurements reported in Figure 29). On the other side, the proposed algorithm recognizes the disturbance and sets to zero the compass readings gain: Figure 30 shows how the control angles increase beyond the threshold values, causing the gain k_2 to decrease and the filter to compute the yaw estimate by integrating the FOG readings (as stated before, this does not cause a relevant deviation of the estimated value on the brief period of time). After the disturbance source is removed and the vehicle is rotated back, the output of the Xsens filter converges to the value estimated by the proposed filter.

Summarizing, if magnetic disturbances are present, the proposed filter proves to be superior to the IMU internal
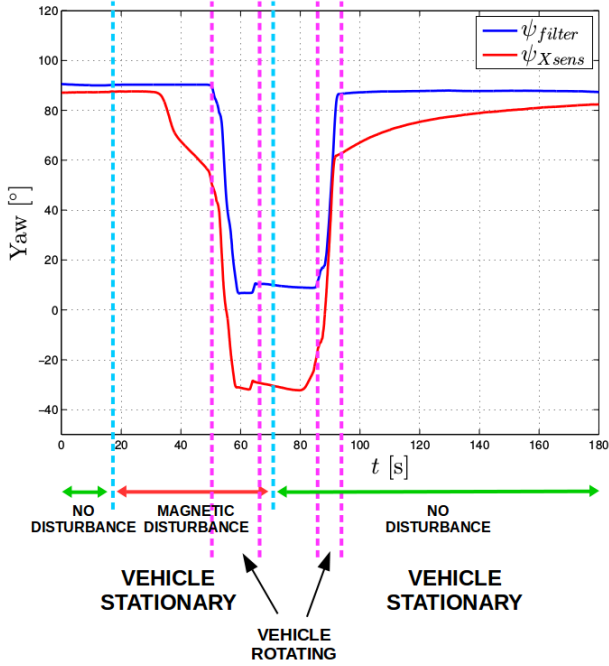
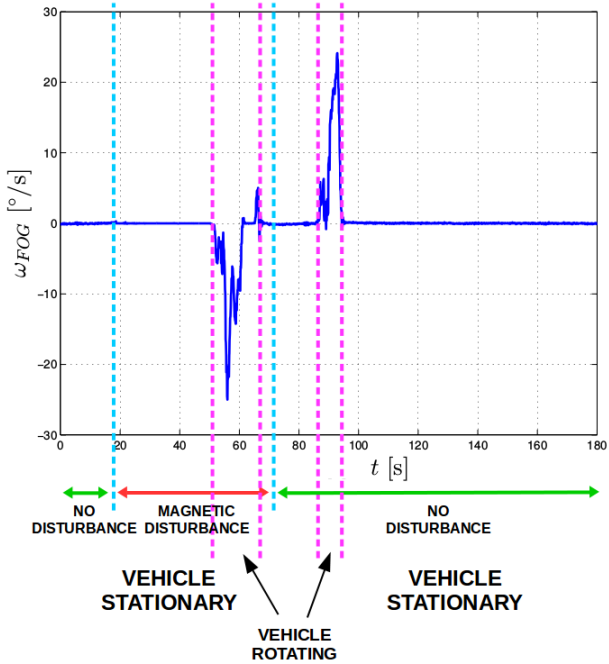Figure 28: Yaw values obtained during the third test.

Figure 29: FOG signal obtained during the third test.

algorithm, offering a more reliable yaw estimate, which constitutes a great benefit to navigation.

6. Conclusion

This paper deals with the problem of correctly estimating the attitude of a mobile robot using a commercial IMU equipped with 3-axis gyroscope, magnetometer and accelerometer. In particular, the field of underwater
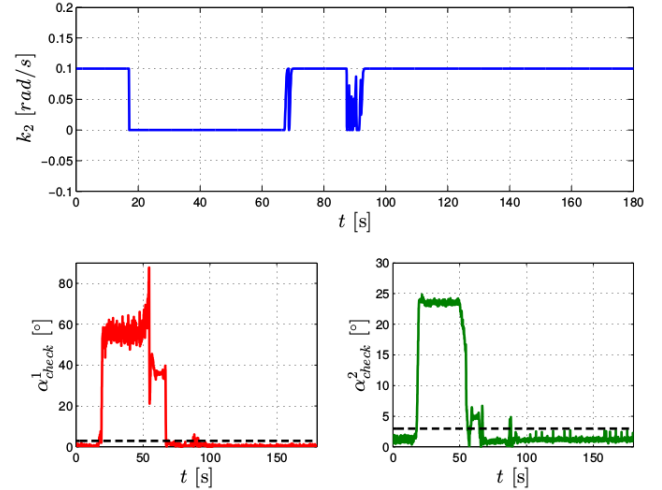

Figure 30: k_2 and control angles values obtained during the third test.

robotics has been considered; however, it is worth to note that the proposed solution is easily adaptable to aerial and terrestrial vehicles. In such applications, the most difficult quantity to determine is the yaw of the vehicle; such measure depends indeed on the magnetometer readings, which are easily susceptible to external disturbances. Thus, special attention has been given to its computation; a fast and simple magnetometer calibration procedure has been illustrated, which is suitable when roll and pitch angles are constrained (this is the case of underwater vehicles), requiring only a turn of the vehicle about the vertical axis to be performed.

An attitude estimation filter for an AUV has been proposed: the solution is indeed based on one of the most used attitude estimation algorithms, presented in [13] by Mahony et al., from which it inherits the structure. Some design changes have been introduced to better adapt the filter for use in the field of underwater robotics. One of the main problems faced is the low reliability of the magnetometer measurements: it has been necessary to *1)* determine a condition which would discriminate correct readings from corrupted ones, and *2)* propose a suitable solution for yaw estimation when compass readings are discarded. Both issues have been addressed with good results.

The resulting filter has been used to estimate the attitude of an AUV, and its performances have been compared with those offered by the estimation algorithm the IMU is equipped with. The results have been very satisfying, highlighting how the proposed filter offers an accurate estimate of the attitude of the vehicle even in the presence of unknown magnetic disturbances; in particular, it has been shown how the presented solution can overcome the problem of the susceptibility of commercial IMUs to magnetic disturbances offering an accurate estimate of the yaw angle, which is fundamental to navigation.

16

Acknowledgements

References

[1] N. Trawny, S.I. Roumeliotis, *Indirect Kalman Filter for Attitude Estimation*, Dept. of Computer Science & Engineering, Technical Report, Vol. 2, Mar. (2005).

[2] J.L. Crassidis, *Sigma-Point Kalman Filtering for Integrated GPS and Inertial Navigation*, AAIA Guidance, Navigation and Control Conference and Exhibit, San Francisco (CA), Aug. 15-18 (2005).

[3] P. Batista, C. Silvestre, P. Oliveira, *Sensor-Based Globally Asymptotic Stable Filters for Attitude Estimation: Analysis, Design, and Performance Evaluation*, IEEE Trans. on Automatic Control, Vol. 57, N. 8, Aug. (2012).

[4] J.L. Crassidis, F.L. Markley, *Predictive Filtering for Attitude Estimation Without Rate Sensors*, Journal of Guidance, Control and Dynamics, Vol. 20, pp. 522-527 (1997).

[5] Hua M.-D., Rudin K., Ducard G., Hamel T., Mahony R., *Nonlinear attitude estimation with measurement decoupling and anti-windup gyro-bias compensation*, in Proceedings of the 18th IFAC World Congress 2011 (IFAC 2011), pp. 2972-2978, Milano (IT), Aug. 28 - Sept. 2 (2011).

[6] Martin P., Salaün E., *Design and implementation of a low-cost observer-based attitude and heading reference system*, Elsevier Control Engineering Practice, Vol. 18, Issue 7, pp. 712-722, July (2010).

[7] Grip T.H., Fossen T.I., Johansen T.A., Saberi A., *A nonlinear Observer for Integration of GNSS and IMU Measurements with Gyro Bias Estimation*, in Proceedings of the American Control Conference, Montreal, Canada, Mar. 24-27 (2012).

[8] Cavallo A., Cirillo A., Cirillo P., De Maria G., Falco P., Natale P., Pirozzi S., *Experimental Comparison of Sensor Fusion Algorithms for Attitude Estimation*, in Proceedings of the 19th IFAC World Congress 2014 (IFAC 2014), Cape Town (SA), Aug. 24-29 (2014).

[9] Kalman R.E., *A New Approach to Linear Filtering and Prediction Problems*, Trans. of the ASME Journal of Basic Engineering, Vol. 82, Series D, pp 35-45 (1960).

[10] Bar-Shalom Y., Li X.R., Kirubarajan T., *Estimation with Applications to Tracking and Navigation: Theory Algorithms and Software*, Wiley, Jul. (2001).

[11] Julier S.J., Uhlmann J.K., *A New extension of the Kalman Filter to Nonlinear Systems*, in Proceedings of the SPIE Signal Processing, Sensor Fusion and Target Recognition VI Conference, Vol. 3068, Jul. 28 (1997).

[12] Euston M., Coote P., Mahony R., Kim J., Hamel T., *A Complementary Filter for Attitude Estimation of a Fixed-Wing UAV*, IEEE/RSJ International Conference on Intelligent Robots and Systems, Nice (FR), Sept. 22-26 (2008).

[13] Mahony R.E., Hamel T., Pflimlin J.M., *Nonlinear Complementary Filters on the Special Orthogonal Group*, IEEE Trans. on Automatic Control, Vol. 53, N. 5, pp 1203-1218 (2008).

[14] Petrich J., Stilwell D.J., *Robust control for an autonomous underwater vehicle that suppresses pitch and yaw coupling*, Ocean Engineering, Vol. 38, Issue 1, pp. 197-204, Jan. (2011).

[15] Akiyama T., Mizuno T., Takasaki M., Ishino Y., Obara K., *Development of a totally active magnetically suspended gyro*, Mechatronics, Vol. 24, Issue 8, pp. 1059-1070, Dec. (2014).

[16] Walker C.R., Stringfield J.Q., Wolbrecht E.T., Anderson M.J., Canning J.R., Bean T.A., Odell D.L., Frenzel J.F., Edwards D.B., *Measurement of the magnetic signature of a moving surface vessel with multiple magnetometer-equipped AUVs*, Ocean Engineering, Vol. 64, Issue 15, pp. 80-87, May (2013).

[17] Allotta B., Costanzi R., Meli E., Pugi L., Ridolfi A., Vettori G., *Cooperative localization of a team of AUVs by a tetrahedral configuration*, Robotics and Autonomous Systems, Vol. 6, N. 8, pp. 1228-1237, Aug. (2014).

[18] Lee H., Jung S., *Balancing and navigation control of a mobile inverted pendulum robot using sensor fusion of low cost sensors*, Mechatronics, Vol. 22, Issue 1, pp. 95-105, Feb. (2012).

[19] Allotta B., Bartolini F., Costanzi R., Monni N., Pugi L., Ridolfi A., *Preliminary design and fast prototyping of an autonomous underwater vehicle propulsion system*, in Proceedings of the Institution of Mechanical Engineers, Part M: Journal of Engineering for the Maritime Environment, Jan. 27 (2014).

[20] Madgwick S.O.H., Harrison A.J.L., Sharkey P.M., Vaidyanathan R., *Measuring motion with kinematically redundant accelerometer arrays: Theory, simulation and implementation*, Mechatronics, Vol. 23, Issue 5, pp. 518-529, Aug. (2013).

[21] Paull L., Saeedi S., Seto M., Li H., *AUV Navigation and Localization: A Review*, IEEE Journal of Oceanic Engineering, Vol. 39, N. 1, Jan. (2014).

[22] Batista P., Silvestre C., Oliveira P., *Attitude and earth velocity estimation - Part I: Globally exponentially stable observer*, IEEE 53rd Annual Conference on Decision and Control (CDC), pp. 121-126, Los Angeles (CA), Dec. 15-17 (2014).

[23] Siciliano B., Khatib O., *Handbook of Robotics*, Springer Handbooks, Napoli and Stanford (2008).

[24] Diamant R., Jin Y., *A Machine Learning Approach for Dead-Reckoning Navigation at Sea Using a Single Accelerometer*, IEEE Journal of Oceanic Engineering, Vol 39, N.4, Oct. (2014).

[25] Chatchanayuenyong T., Parnichkun M., *Neural network based-time optimal sliding mode control for an autonomous underwater robot*, Mechatronics, Vol 16, Issue 8, pp. 471-478, Oct. (2006).

[26] Turner D.A., Anderson I.J., Mason J.C., Cox M.G., *An Algorithm for Fitting an Ellipsoid to Data*, Dec. (1999).

[27] Fitzgibbon A., Pilu M., Fisher R.B., *Direct Least Square Fitting of Ellipses*, IEEE Trans. on Pattern Analysis and Machine Intelligence, Vol. 21, N. 5, May (1999).

[28] Halíř R., Flusser J., *Numerically Stable Direct Least Square Fitting of Ellipses*, WSCG International Conference in Central Europe on Computer Graphics and Visualization (1998).

[29] National Geophysics Data Center, *http://www.ngdc.noaa.gov*

[30] Miller P.A., Farrell J.A., Zhao Y., Djapic V., *Autonomous Underwater Vehicle Navigation*, IEEE Journal of Oceanic Engineering, Vol. 35, N. 3, Jul. (2010).

[31] Lee P.-M., Jun B.-H., *Pseudo long base line navigation algorithm for underwater vehicles with inertial sensors and two acoustic range measurements*, Ocean Engineering, Vol. 34, Issues 3-4, pp. 416-425, Mar. (2007).

[32] Robot Operating System, *http://www.ros.org*

[33] Allotta B., Costanzi R., Ridolfi A. et al., *The ARROWS project: adapting and developing robotics technologies for underwater archaeology*, IFAC Workshop on Navigation and Control of Underwater Vehicles (NGCUV 2015), Girona, Spain, April (2015).